and a charge order (*12*, *13*). Therefore, it would be tempting to assume that at least a portion of the measured gap is due to the charge order, in analogy with conventional two-dimensional (2D) charge density wave (CDW) systems. It has been suggested that, in cuprates, the spin-charge–ordered state forms in a way where carriers doped into the AF insulator segregate into 1D charge-rich structures (stripes) separated by the charge-poor regions of a parent antiferromagnet (*14*, *23*–*25*). However, questions have often been raised on how to reconcile these unidirectional structures with an apparent 2D Fermi surface and a gap with *d*-wave symmetry. In the more conventional view, doped carriers are delocalized in the planes, forming a 2D Fermi surface that grows in proportion with carrier concentration. The charge-spin–ordered state may then be formed in the particle-hole channel by nesting of Fermi surface segments, producing a divergent electronic susceptibility and a Peierls-like instability and pushing the system into a lower energy state with a single-particle gap at nested portions of the Fermi surface. An example of a cuprate where such a "nesting" scenario is proposed to be at play is $Ca_{2-x}Na_xCuO_2Cl_2$ (CNCOC) (*26*). STM studies have detected checkerboard-like modulations in local DOS on the surface of this material, with $4a \times 4a$ periodicity, independent of doping (*27*). Subsequent ARPES studies on the same system have shown a Fermi surface with a nodal arc and truncated antinodal segments (*26*). The antinodal segments can be efficiently nested by the charge-ordering wave vectors $q_{CDW} = 2k_F = \pi/(2a)$ and $3\pi/(2a)$, observed in STM for charge superstructure, making the nesting scenario viable, at least near the surface of CNCOC. Here, $k_F$ represents the antinodal Fermi wave vector. However, if we apply the same nesting scenario to LBCO at $x = 1/8$, we obtain $q_{CDW} \approx 4k_F$ ($= \pi/2a$) for charge order instead of $2k_F$ nesting, which is suggested to be at play in CNCOC. Moreover, the nesting of antinodal segments would produce a wave vector that shortens with doping, opposite of that observed in neutron-scattering studies in terms of magnetic incommensurability. This result is illustrated in Fig. 4, where we compile the doping dependences of several relevant quantities.

There is another, more fundamental problem with the nesting scenario: Any order originating from nesting (particle-hole channel) would open a gap only on nested segments of the Fermi surface, preserving the non-nested regions. The fact that only four gapless points (nodes) remain in the ground state essentially rules out nesting as an origin of the pseudogap. In addition, a gap caused by conventional spin-charge order would be pinned to the Fermi level only in special cases. The observation that the gap is always pinned to the Fermi level (independent of *k*-point, as measured in ARPES and of doping level, as seen in STM on different materials) and that it has *d*-wave symmetry undoubtedly points to its pairing origin [interaction in the particle-particle singlet channel (*28*)]. In contrast to the low-energy pairing gap, STM at higher energies shows a DOS suppressed in a highly asymmetric manner, indicating that some of the nesting-related phenomena might be at play at these higher energies (Fig. 3B).

The unexpected anticorrelation of the low-energy pairing gap and $T_C$ over some region of the phase diagram suggests that, in the state with strongly bound Cooper pairs, the phase coherence is strongly suppressed by quantum phase fluctuations. Cooper pairs are then susceptible to spatial ordering and may form various unidirectional (*14*, *24*, *25*) or 2D (*15*, *27*–*30*) superstructures. Quantum phase fluctuations are particularly prominent in cases where such superstructures are anomalously stable. For some of the proposed structures, this occurs at the doping of $1/8$, in general agreement with our results: $1/8$ represents the most prominent "magic fraction" for a checkerboard-like "CDW of Cooper pairs" (*15*), and it locks the stripes to the lattice in a unidirectional alternative. The presence of nodes in the ground state of the pseudogap represents a new decisive test for validity of models proposed to describe such structures.

### References and Notes


1. T. Timusk, B. Statt, *Rep. Prog. Phys.* **62**, 61 (1999).
2. A. Damascelli, Z. Hussain, Z.-X. Shen, *Rev. Mod. Phys.* **75**, 473 (2003).
3. G. Baskaran, Z. Zou, P. W. Anderson, *Solid State Commun.* **63**, 973 (1987).
4. P. A. Lee, N. Nagaosa, X.-G. Wen, *Rev. Mod. Phys.* **78**, 17 (2006).
5. E. W. Carlson, V. J. Emery, S. A. Kivelson, D. Orgad, *The Physics of Superconductivity: Conventional and Unconventional*, vol. 2, K. H. Benneman, J. B. Ketterson, Eds. (Springer, Berlin, 2003).
6. M. Franz, Z. Tešanović, *Phys. Rev. Lett.* **87**, 257003 (2001).
7. V. J. Emery, S. A. Kivelson, *Nature* **374**, 434 (1995).
8. B. Lake *et al.*, *Science* **291**, 1759 (2001).
9. J. E. Hoffman *et al.*, *Science* **295**, 466 (2002).
10. M. Vershinin *et al.*, *Science* **303**, 1995 (2004).
11. K. McElroy *et al.*, *Phys. Rev. Lett.* **94**, 197005 (2005).
12. J. M. Tranquada *et al.*, *Nature* **429**, 534 (2004).
13. P. Abbamonte *et al.*, *Nat. Phys.* **1**, 155 (2005).
14. J. M. Tranquada, B. J. Sternlieb, J. D. Axe, Y. Nakamura, S. Uchida, *Nature* **375**, 561 (1995).
15. Z. Tešanović, *Phys. Rev. Lett.* **93**, 217004 (2004).
16. A. R. Moodenbaugh, Y. Xu, M. Suenaga, T. J. Folkerts, R. N. Shelton, *Phys. Rev. B* **38**, 4596 (1988).
17. C. C. Homes *et al.*, *Phys. Rev. Lett.* **96**, 257002 (2006).
18. X. J. Zhou *et al.*, *Phys. Rev. Lett.* **92**, 187001 (2004).
19. Materials and methods are available as supporting material on *Science* Online.
20. M. R. Norman *et al.*, *Nature* **392**, 157 (1998).
21. A. Kanigel *et al.*, *Nat. Phys.* **2**, 447 (2006).
22. M. Sutherland *et al.*, *Phys. Rev. Lett.* **94**, 147004 (2005).
23. J. Zaanen, O. Gunnarson, *Phys. Rev. B* **40**, 7391 (1989).
24. V. J. Emery, S. A. Kivelson, *Physica C* **235-240**, 189 (1994).
25. M. Granath, V. Oganesyan, S. A. Kivelson, E. Fradkin, V. J. Emery, *Phys. Rev. Lett.* **87**, 167011 (2001).
26. K. M. Shen *et al.*, *Science* **307**, 901 (2005).
27. T. Hanaguri *et al.*, *Nature* **430**, 1001 (2004).
28. M. Franz, *Science* **305**, 1410 (2004).
29. H.-D. Chen, O. Vafek, A. Yazdani, S.-C. Zhang, *Phys. Rev. Lett.* **93**, 187002 (2004).
30. D. Podolsky, E. Demler, K. Damle, B. I. Halperin, *Phys. Rev. B* **67**, 094514 (2003).
31. M. Fujita *et al.*, *Phys. Rev. B* **65**, 064505 (2002).
32. J. M. Tranquada *et al.*, *Phys. Rev. Lett.* **78**, 338 (1997).


33. The authors thank P. Anderson, A. Chubukov, E. Fradkin, C. Homes, P. Johnson, S. Kivelson, W. Ku, A. Millis, Z. Tešanović, A. Tsvelik, and J. Tranquada for useful discussions and Z-H. Pan for technical help. T.V., A.V.F., and G.D.G. are supported by the Office of Science, U.S. Department of Energy (DOE). J.C.D and J.L. are supported by the Office of Science, DOE, the Office of Naval Research, and by Cornell University.


### Supporting Online Material

www.sciencemag.org/cgi/content/full/1134742/DC1
Materials and Methods
Figs. S1 and S2
References


5 September 2006; accepted 3 November 2006
Published online 16 November 2006;
10.1126/science.1134742
Include this information when citing this paper.


# Nondestructive Optical Measurements of a Single Electron Spin in a Quantum Dot


**J. Berezovsky, M. H. Mikkelsen, O. Gywat, N. G. Stoltz, L. A. Coldren, D. D. Awschalom***



**Kerr rotation measurements on a single electron spin confined in a charge-tunable semiconductor quantum dot demonstrate a means to directly probe the spin off-resonance, thus minimally disturbing the system. Energy-resolved magneto-optical spectra reveal information about the optically oriented spin polarization and the transverse spin lifetime of the electron as a function of the charging of the dot. These results represent progress toward the manipulation and coupling of single spins and photons for quantum information processing.**


The prospect of quantum computation in conventional material systems has spurred much research into the physics of carrier spins in semiconductor quantum dots (QDs) (*1*). An important element necessary for spin-based quantum computing is the readout of the qubit spin state. Previously demonstrated schemes for single spin readout in a QD include optical measurements, such as photoluminescence (PL) polarization (*2*, *3*) or polarization-dependent absorption (*4*–*6*). Single spins can also be read out electrically by measuring the spin-dependent probability for an electron to tunnel out of the


Center for Spintronics and Quantum Computation, University of California, Santa Barbara, CA 93106, USA.

*To whom correspondence should be addressed. E-mail: awsch@physics.ucsb.edu

dot (*7*). However, these methods are destructive, in that they either remove the spin from the dot or drive transitions in the system with a resonant optical field. In contrast, we describe measurements of a single electron spin using Kerr rotation (KR), in which the spin state is probed nonresonantly, thus minimally disturbing the system. This effective spin-photon interaction has been shown to allow for Schrödinger's cat–type measurements to probe quantum effects such as measurement-induced decoherence and spin squeezing (*8*, *9*), as well as the implementation of quantum information protocols involving spin-photon entanglement (*10*) and optically mediated spin-spin entanglement (*11*–*13*).

In the present work, the electrons were confined to a single charge-tunable QD formed by monolayer fluctuations at the interfaces of a gallium arsenide (GaAs) quantum well (QW). The QD layer was centered within an optical microcavity with a resonance chosen to enhance the interaction of the optical field with the QD at energies well below the lowest interband transition. By the application of a transverse magnetic field, the electron spins can be depolarized in a Hanle-type measurement, thereby yielding information about the spin lifetime.

The magneto-optical Kerr effect results in a rotation of the plane of polarization of linearly polarized light with energy $E$ upon reflection off the sample and is analogous to the Faraday effect for transmitted light. For both effects, the rotation angle is determined by the difference of the dynamic dielectric response functions for left and right ($\sigma^+$ and $\sigma^-$) circularly polarized light, which are proportional to the interband momentum matrix elements $\langle\psi_c|\hat{p}_x \pm i\hat{p}_y|\psi_v\rangle$, where $\psi_c$ ($\psi_v$) is a conduction (valence) band state (*14*, *15*), and $\hat{p}_x$ and $\hat{p}_y$ are the components of the electron momentum operator perpendicular to the growth direction. As a result of the microcavity, both reflection and transmission contribute to the measured polarization rotation. For simplicity, we refer only to KR. For a single conduction-band energy level in a QD containing a spin-up electron in a state $|\psi_\uparrow\rangle$, optical transitions to the spin-up state are Pauli-blocked, and the KR angle $\theta_K$ is then given by

$$\theta_K(E) = CE \sum_{\alpha=\pm1;v} \alpha|\langle\psi_\downarrow|\hat{p}_x + \alpha i\hat{p}_y|\psi_v\rangle|^2 \frac{E - E_{0,v}}{(E - E_{0,v})^2 + \Gamma_v^2} \quad (1)$$

where $C$ is a constant, and $E_{0,v}$ and $\Gamma_v$ are the energy and linewidth of the transition involving $|\psi_v\rangle$, respectively. We focus on a single transition in the sum in Eq. 1 and drop the index v. For $\Gamma << |\Delta| << E$, where $\Delta = E - E_0$, we note that $\theta_K \sim \Delta^{-1}$, which decays slower than the absorption line ($\sim\Delta^{-2}$) (*15*, *16*). Therefore, for a suitable detuning $\Delta$, KR can be detected whereas photon absorption is strongly suppressed.

The sample structure (Fig. 1A) is grown by molecular beam epitaxy and consists of a single 4.2-nm GaAs QW in the center of a planar aluminum GaAS ($Al_{0.3}Ga_{0.7}As$) λ-cavity (*17*). The reflectivity of the sample at 10 K (Fig. 1D) shows a cavity resonance centered at 763.6 nm (1.624 eV) with a quality factor of 120. The probe light effectively interacts with the spin many times as it is reflected back and forth within the cavity. As a result, the polarization rotation described by Eq. 1 occurs repeatedly, enhancing the small, single spin KR angle (*18*). Based on previous measurements with similar cavities (*19*, *20*), we expect the KR at the peak of the cavity resonance to be enhanced by a factor of ~15.

The band profile for our structure (*17*), calculated with a one-dimensional self-consistent Poisson-Schrödinger solver, is shown in Fig. 1B. By the application of a bias voltage $V_b$ across the structure, the conduction-band minimum in the QW can be made to plunge beneath the Fermi level, charging first the QDs, then the well itself (*21*, *22*). The onset of this charging occurs around 0.5 V (Fig. 1C) according to the band-structure calculation.

A continuous wave (cw) Ti-sapphire laser (1.654 to 1.662 eV) is focused through a microscope objective (spot size ~ 2 μm) on the sample at temperature $T$ = 10 K to excite electron-hole pairs into the continuum of states in the QW. The carriers then relax into the QDs, and the subsequent PL is collected through the same objective, dispersed in a spectrometer, and detected by a liquid nitrogen–cooled charge-coupled device. In a typical single-dot PL spectrum as a function of the applied bias (Fig. 2A), the sharp features (linewidth ~100 μeV) are characteristic of single-dot PL (*23*), demonstrating the presence of only one QD within the laser focus. Above 0.5 V, a single line is observed at 1.6297 eV, which is attributed to recombination from the negatively charged exciton (trion or $X^-$) state. Below 0.5 V, this line persists faintly, and a bright line appears 3.6 meV higher in energy because of the neutral exciton ($X^0$) transition. The presence of the $X^-$ line at $V_b < 0.5$ V implies that occasionally a single electron is trapped in the dot, forming an $X^-$ when binding to an electron and a hole. In addition, a faint line at 1.6292 eV is visible from radiative decay of the biexciton (XX). These assignments of the observed lines are consistent with measurements on

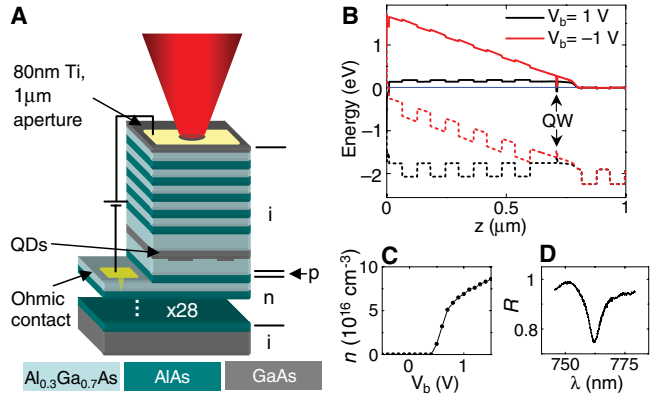


**Fig. 1.** Sample structure and characterization. (**A**) Schematic of the sample structure. i, n, and p indicate intrinsic (undoped), n-doped, and p-doped regions of the sample, respectively. Twenty-eight repetitions of the AlAs/AlGaAs layers, indicated by x28, are not shown. AlAs, aluminum arsenide. (**B**) The calculated conduction (valence) band profile along the growth direction z shown in solid (dashed) lines. Raising the bias voltage $V_b$ from −1 to 1 V lowers the QW conduction-band minimum past the Fermi level (blue). (**C**) The calculated electron density $n$ in the QW showing the onset of charging at $V_b$ = 0.5 V. (**D**) The reflectivity $R$ of the cavity at $T$ = 10 K versus wavelength λ, with a resonance at 763.6 nm.

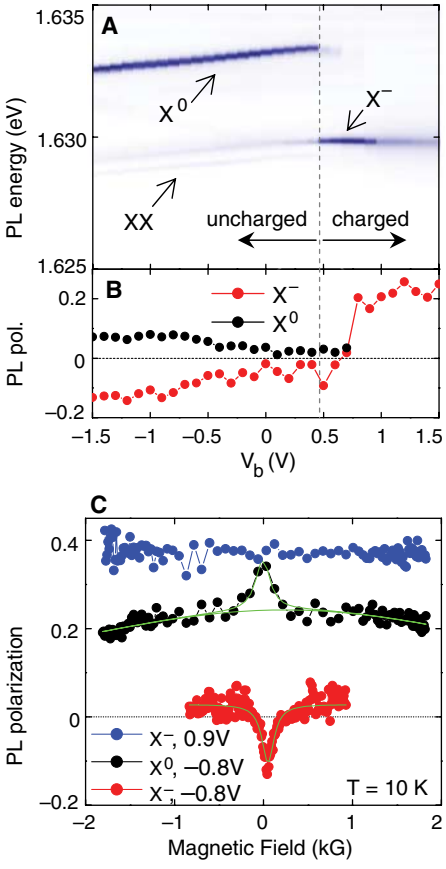


**Fig. 2.** Single-dot PL and Hanle measurements. (**A**) PL of a single QD as a function of $V_b$. A jump in the PL energy indicates the onset of QD charging. (**B**) The polarization (pol.) of the $X^-$ and $X^0$ PL lines as a function of bias. (**C**) Hanle curves in the charged regime (blue) and in the uncharged regime (black and red).

similar structures (*2*, *22*) and are further supported by the linear dependence of the $X^-$ and $X^0$ lines and the quadratic dependence of the XX line on the excitation intensity. Figure 3C illustrates these three optical transitions. In this QD, we see no evidence of a positively charged exciton.

With circularly polarized excitation, spin-polarized electrons and heavy holes can be pumped into the QD because of the optical selection rules of the GaAs QW (*2*, *24*). For the purposes of this discussion, spin polarization parallel to the optically injected electron spin polarization will be referred to as "spin up" and the opposite spin as "spin down." Information about the spin polarization in the QD can be gained from the polarization of the PL (*2*). The circular polarization of the PL is determined by switching the helicity of the pump from $\sigma^+$ to $\sigma^-$ and measuring the intensity of the $\sigma^+$-polarized PL ($I^+$ and $I^-$, respectively). The polarization is then defined as $P = (I^+ - I^-)/(I^+ + I^-)$ and is shown for the $X^0$ and $X^-$ lines in Fig. 2B, in agreement with earlier results (*2*, *22*).

The polarization of the $X^-$ line is determined by the hole spin, as the two electrons in the trion form a spin-singlet state. In the uncharged regime ($V_b < 0.5$ V), the negative polarization of the $X^-$ PL indicates that the heavy hole undergoes a spin flip before recombination in most cases. Hole spin flips may occur either during energy relaxation in the QW (*25*) or by an exchange-mediated electron-hole spin flip (*26*). Regardless of the hole spin-flip process, after the recombination of the $X^-$, the electron left in the QD is polarized in the spin-up direction. In this way, both optical injection and trion recombination serve to pump lone spin-up electrons into the QD.

When the dot is initially charged near $V_b$ = 0.5 V, the now dominant $X^-$ line remains negatively polarized, resulting in continued pumping of the spin-up state. As the electron density in the QW increases with higher applied bias, the $X^-$ polarization becomes positive, as has been previously observed (*2*, *22*).

In a transverse applied magnetic field, the electron spins precess, depolarizing the PL. The hole spins do not precess (*27*) because the heavy and light hole states are split [by ~20 meV in our sample (*28*)], leading to an effective heavy-hole $g$ factor of zero in the plane of the QW. Hanle measurements on this dot are summarized in Fig. 2C. In the charged regime, at $V_b$ = 0.9 V, no depolarization of the $X^-$ PL is observed, as expected for polarization resulting from the hole spin. The case is markedly different at $V_b$ = –0.8 V, in the uncharged regime. Here, the (negatively polarized) $X^-$ line is depolarized with a half-width $B_{1/2}$ = 80 G. With an estimated electron $g$ factor of $g_e$ = 0.2 (*2*), $B_{1/2}$ = 80 G corresponds to a time-averaged transverse spin lifetime $T_2^* = \hbar/B_{1/2}g_e\mu_B$ = 7 ns, where $\mu_B$ is the Bohr magneton and $\hbar$ is Planck's constant $h$ divided by $2\pi$. This sharp Hanle peak has been previously attributed to the electron spin in the QD, before $X^-$ formation (*2*). The $X^0$ line shows a much broader peak ($B_{1/2}$ = 4.1 kG), with a small narrow component at low field. The broad component is consistent with the radiative lifetime of the exciton (~50 ps) (*4*). The narrow component has a $B_{1/2}$ = 95 G, which is similar to the $X^-$ width. Indeed, this narrow peak is expected if a lone electron in the dot can bind and recombine with a subsequently injected hole. Similar features have been observed in ensemble Hanle measurements in GaAs QWs (*29*).

In the uncharged regime, spin-polarized excitons or electrons can be pumped into the dot. Both optical injection and trion recombination

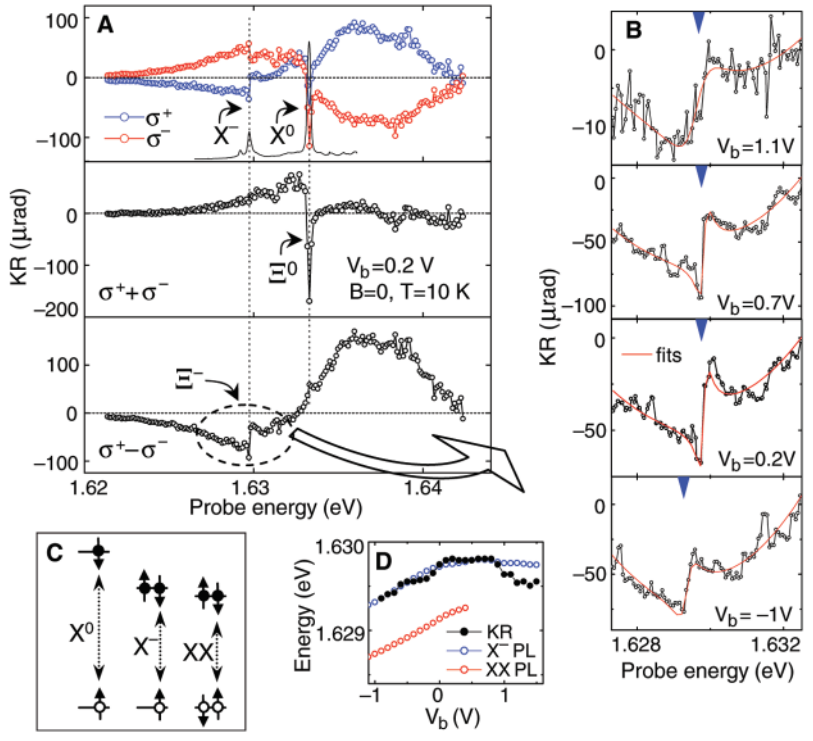


**Fig. 3.** Single-dot KR spectra. (**A**) Top panel, KR measured with a $\sigma^+$- and $\sigma^-$-polarized pump at $V_b$ = 0.2 V. The PL at this bias is also shown. Middle panel, the sum of the $\sigma^+$ and $\sigma^-$ data showing a spin-independent feature $\Xi^0$ at the $X^0$ energy. Bottom panel, the difference of the $\sigma^+$ and $\sigma^-$ data with the feature $\Xi^-$ at the $X^-$ energy circled. The circled feature is shown in more detail in (**B**), as indicated by the large arrow. (**B**) Single spin KR ($\Xi^-$) at various bias voltages. The blue triangle indicates the energy of the $X^-$ PL line. Fits to the data are shown in red. (**C**) Illustration of three relevant optical transitions. Solid circles represent electrons, and open circles represent holes. (**D**) The agreement between the $X^-$ PL energy and the $\Xi^-$ energy. The biexciton PL energy is also shown for comparison.

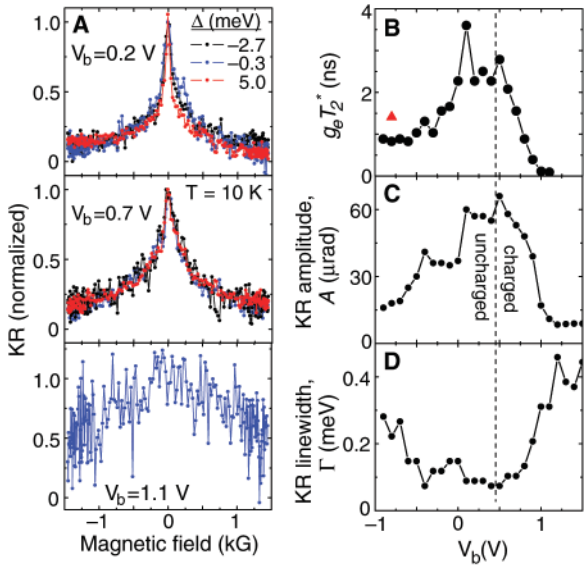


**Fig. 4.** KR depolarization and analysis. (**A**) KR as a function of transverse magnetic field for various bias voltages. The top two panels show measurements with the probe at various detunings Δ from the $X^-$ energy. (**B**) $g_eT_2^*$ determined from the KR half-width. The red triangle indicates the value obtained from the Hanle measurement. (**C** and **D**) The amplitude and width of the KR $\Xi^-$ feature as a function of applied bias.

serve to pump spin-up electrons. At high bias in the charged regime ($V_b$ = 0.9 V), the PL polarization is due to the hole spin, obscuring any information about the electron spin polarization. To address this issue, we require a more direct probe of the spin polarization.

To probe spins in the dot through KR, we focused a second, linearly polarized, cw Ti-sapphire laser onto the sample, spatially overlapping the pump laser (*17*). The data in the top panel of Fig. 3A show the KR signal as a function of probe energy for $\sigma^+$ and $\sigma^-$ pump helicity. Here, the applied bias is $V_b$ = 0.2 V and the QD is in the uncharged regime. The PL at this bias is also shown, with the $X^-$ and $X^0$ energies indicated by the dotted lines. These energies coincide spectrally with two sharp features observed in the KR data, which we will refer to as $\Xi^-$ and $\Xi^0$, respectively. In the bottom two panels of Fig. 3A, the sum and difference of the $\sigma^+$ and $\sigma^-$ data are shown. The feature $\Xi^0$ at the $X^0$ energy clearly does not depend on the sign of the injected spin and is similar to features seen in single-dot absorption measurements (*30*). We attribute this peak to polarization-dependent absorption in the QD. We focus here on the ($\sigma^+$–$\sigma^-$) data, which represent KR due to the optically oriented spin polarization. The feature $\Xi^-$ at the $X^-$ energy only appears in the difference data, indicating that it is due to the injected spin polarization, shown in Fig. 3B at four different bias voltages. For all voltages, the $\Xi^-$ feature is centered at the $X^-$ transition energy, indicated by the blue triangles. We can fit these data to Eq. 1 including only a single transition in the sum, on top of a broad background (red lines, Fig. 3B). From the free parameters in these fits, we determine the transition energy $E_0$, amplitude $A$ (defined as half the difference of the local maximum and minimum near $E_0$), and width $\Gamma$ of the $\Xi^-$ KR feature.

Figure 3D shows $E_0$ compared to the energy of the $X^-$ PL line as a function of the applied bias. The two energies agree well and show the same quantum-confined Stark shift. Only at the highest bias, where substantial broadening sets in, do we observe a small anti-Stokes shift between $E_0$ and the $X^-$ PL energy. This effect may be caused by interactions with electrons in the QW. For a single electron spin in the QD ground state, the lowest-energy optical transition contributing in Eq. 1 is the $X^-$ transition (Fig. 3C). Thus, the $\Xi^-$ KR feature is due to the measurement of a single electron spin in the QD. We have repeated this measurement on another QD and observed the same $\Xi^-$ feature, also at the $X^-$ PL energy. The large, broad KR background is likely due to transitions involving excited electron and hole states, which are typically a few milli–electron volts above the lowest transition (*23*).

If present, a KR feature due to the $X^0$ spin should appear centered at the XX transition energy. The signal-to-noise ratio in our measurement is not high enough to conclusively identify such a feature. Despite the large amplitude of the $X^0$ PL compared to the $X^-$ PL in the uncharged bias regime (~10:1), the short radiative lifetime of the $X^0$ state results in a low steady-state $X^0$ population and therefore in a low KR signal.

By applying a transverse magnetic field $B$, we can monitor the depolarization of the single electron spin through the KR signal. In contrast to the Hanle measurements described above, the KR probes the spin in the QD directly and nondestructively, as opposed to being inferred from the spin-dependent formation of the $X^-$. The KR as a function of $B$ is shown for three different bias voltages (Fig. 4A). At $V_b$ = 0.2 V, in the uncharged regime, a narrow peak is observed with a $B_{1/2}$ = 52 G, which is consistent with the $X^-$ Hanle width measured in this regime. At $V_b$ = 0.7 V, where the dot has charged but the PL remains negatively polarized, we measure a somewhat wider KR depolarization curve, with $B_{1/2}$ = 150 G. When the QW is charged further, the spin lifetime decreases as shown at $V_b$ = 1.1 V, with $B_{1/2}$ = 1.4 kG. Assuming an effective electron $g$ factor of 0.2 (*2*), these half-widths correspond to transverse spin lifetimes of 11, 3.3, and 0.8 ns, respectively.

The electron spin depolarization curves measured at probe energies detuned from the $X^-$ transition by an energy $\Delta$ are shown in the top two panels of Fig. 4A for $\Delta$ = –0.3 meV (at the maximum of the $\Xi^-$ feature), $\Delta$ = –2.7 meV (in the low-energy tail), and $\Delta$ = +5.0 meV (on the broad, high-energy feature). The curves have been normalized by their peak values, which vary with probe energy, but show identical lineshapes for a given bias. This suggests that, in this entire range of detuning, the KR of the same spin-polarized electron state in the QD is being probed.

Figure 4B shows $g_eT_2^* = \hbar/B_{1/2}\mu_B$ as a function of the applied bias, measured at a probe energy $E$ = 1.6288 eV, near the $X^-$ transition. The dashed line indicates the onset of QD charging. The spin lifetime is largest in the uncharged regime. Here, $g_eT_2^* \sim 3$ ns is consistent with previous measurements (*2*) in which the spin dephasing is attributed to the random, fluctuating hyperfine field (*31*, *32*). As the dot and well are charged, the electron spin lifetime decreases dramatically. This result can be caused by the increasingly rapid capture of a second electron in the dot, which forms a spin-zero singlet state. Also, as discussed below, spin flips with electrons in the QW are likely to be a relevant mechanism in this regime.

The amplitude of the $\Xi^-$ KR signal is shown as a function of $V_b$ (Fig. 4C). $A$ decreases in the charged regime, reflecting the lower spin lifetime. We have argued above that spin-up electrons are pumped into the QD in the uncharged regime. Therefore, the constant sign of the KR over the entire range of bias indicates spin-up polarization in the charged regime as well. Contrary to this observed polarization, the positively polarized $X^-$ PL leaves a spin-down electron in the QD. However, this electron interacts with the bath of electrons in the QW, which is, on average, optically oriented in the spin-up direction. The predominant spin in the QW may be transferred to the electron in the dot via a higher-order tunneling process (*33*). The finite spin-up polarization measured up to a large bias suggests that these electron-electron spin flips dominate over the $X^-$–mediated spin pumping in the charged regime.

As the bias increases above $V_b$ = 0.5 V, the width of the $\Xi^-$ KR feature, $\Gamma$, grows by a factor of six, as shown in Fig. 4D. A similar increase in linewidth is seen in the $X^-$ PL in the charged regime. This provides further evidence for an increased coupling of the QD to other electronic states as the charging increases.

By probing a single electron in a QD through KR nonresonantly, we demonstrate a direct measurement of the electron spin with minimal perturbation to the system. As a first application, this method reveals information about spin dynamics in single QDs and constitutes a pathway toward quantum nondemolition measurements and optically mediated entanglement of single spins in the solid state. This scheme may also prove useful for nondestructive measurements in a variety of solid-state qubits, such as electrically gated (*7*) or chemically synthesized (*20*) QDs.

### References and Notes


1. D. D. Awschalom, D. Loss, N. Samarth, Eds., *Semiconductor Spintronics and Quantum Computation* (Springer, Berlin, 2002).
2. A. S. Bracker *et al.*, *Phys. Rev. Lett.* **94**, 047402 (2005).
3. A. Ebbens *et al.*, *Phys. Rev. B* **72**, 073307 (2005).
4. T. H. Stievater *et al.*, *Appl. Phys. Lett.* **81**, 4251 (2002).
5. X. Li, Y. Wu, D. G. Steel, D. Gammon, L. J. Sham, *Phys. Rev. B* **70**, 195330 (2004).
6. A. Högele *et al.*, *Appl. Phys. Lett.* **86**, 221905 (2005).
7. J. M. Elzerman *et al.*, *Nature* **430**, 431 (2004).
8. J. M. Geremia, J. K. Stockton, H. Mabuchi, *Science* **304**, 270 (2004).
9. A. Kuzmich, L. Mandel, N. P. Bigelow, *Phys. Rev. Lett.* **85**, 1594 (2000).
10. F. Meier, D. D. Awschalom, *Phys. Rev. B* **70**, 205329 (2004).
11. B. Julsgaard, A. Kozhekin, E. S. Polzik, *Nature* **413**, 400 (2001).
12. M. N. Leuenberger, M. E. Flatté, D. D. Awschalom, *Phys. Rev. Lett.* **94**, 107401 (2005).
13. M. N. Leuenberger, *Phys. Rev. B* **73**, 075312 (2006).
14. D. V. Kupriyanov, I. M. Sokolov, *Quantum Opt.* **4**, 55 (1992).
15. F. Meier, D. D. Awschalom, *Phys. Rev. B* **71**, 205315 (2005).
16. J. R. Guest *et al.*, *Phys. Rev. B* **65**, 241310(R) (2002).
17. Materials and methods are available as supporting material on *Science* Online.
18. M. Sugita, S. Machida, Y. Yamamoto, preprint available at http://arXiv.org/abs/quant-ph/0301064.
19. G. Salis, M. Moser, *Phys. Rev. B* **72**, 115325 (2005).
20. Y. Q. Li *et al.*, *Appl. Phys. Lett.* **88**, 193126 (2006).
21. R. J. Warburton *et al.*, *Nature* **405**, 926 (2000).
22. A. S. Bracker *et al.*, *Phys. Rev. B* **72**, 035332 (2005).
23. D. Gammon, E. S. Snow, B. V. Shanabrook, D. S. Katzer, D. Park, *Science* **273**, 87 (1996).
24. F. Meier, B. Zakharchenya, Eds., *Optical Orientation: Modern Problems in Condensed Matter Sciences* (North Holland, Amsterdam, 1984).
25. R. I. Dzhioev *et al.*, *Phys. Solid State* **40**, 1587 (1998).
26. S. Cortez *et al.*, *Phys. Rev. Lett.* **89**, 207401 (2002).
27. J. G. Tischler, A. S. Bracker, D. Gammon, D. Park, *Phys. Rev. B* **66**, 081310(R) (2002).
28. Y. El Khalifi, B. Gil, H. Mathieu, T. Fukunaga, H. Nakashima, *Phys. Rev. B* **39**, 13533 (1989).

29. R. I. Dzhioev *et al.*, *Phys. Rev. B* **66**, 153409 (2002).
30. A. Zrenner *et al.*, *Phys. Rev. Lett.* **72**, 3382 (1994).
31. A. V. Khaetskii, D. Loss, L. Glazman, *Phys. Rev. Lett.* **88**, 186802 (2002).
32. I. A. Merkulov, Al. L. Efros, M. Rosen, *Phys. Rev. B* **65**, 205309 (2002).
33. J. Lehmann, D. Loss, *Phys. Rev. B* **73**, 045328 (2006).
34. We thank Y. K. Kato for useful advice and discussions and acknowledge support from NSF and the Air Force Office of Scientific Research.

**Supporting Online Material**
www.sciencemag.org/cgi/content/full/1133862/DC1
Materials and Methods
References

14 August 2006; accepted 1 November 2006
Published online 9 November 2006;
10.1126/science.1133862
Include this information when citing this paper.

# A Sea-Floor Spreading Event Captured by Seismometers

**M. Tolstoy,[1]* J. P. Cowen,[2] E. T. Baker,[3] D. J. Fornari,[4] K. H. Rubin,[5] T. M. Shank,[4] F. Waldhauser,[1] D. R. Bohnenstiehl,[1] D. W. Forsyth,[6] R. C. Holmes,[1] B. Love,[7] M. R. Perfit,[8] R. T. Weekly,[1] S. A. Soule,[4] B. Glazer[2]**

**Two-thirds of Earth's surface is formed at mid-ocean ridges, yet sea-floor spreading events are poorly understood because they occur far beneath the ocean surface. At 9°50'N on the East Pacific Rise, ocean-bottom seismometers recently recorded the microearthquake character of a mid-ocean ridge eruption, including precursory activity. A gradual ramp-up in activity rates since seismic monitoring began at this site in October 2003 suggests that eruptions may be forecast in the fast-spreading environment. The pattern culminates in an intense but brief (~6-hour) inferred diking event on 22 January 2006, followed by rapid tapering to markedly decreased levels of seismicity.**

The ocean floor is episodically created by injections of magma in dikes that commonly erupt along divergent boundaries that separate tectonic plates. The timing and mechanics of these sea-floor spreading events must normally be inferred from remote seismic or hydroacoustic data and from sea-floor geology. Along fast-spreading ridges, most on-axis seismicity is too small in local magnitude (<2 $M_L$) to be recorded by global seismic networks or regional hydrophone arrays (*1*). A long-standing goal of mid-ocean ridge (MOR) research has been to capture the seismic precursors, signature, and aftermath of a sea-floor spreading event and eruption within a network of ocean-bottom seismometers (OBSs).

The East Pacific Rise (EPR) near 9°50'N spreads at a full rate of ~110 mm year$^{-1}$ (*2*) and is one of the best-studied MOR segments in the world. Ever since an eruption was documented in 1991 (*3*, *4*), scientists have regularly returned to document ecosystem progression (*5*, *6*), to study changes in vent-fluid chemistry and temperature (*7*, *8*), and to conduct detailed geological mapping (*9*). Based on the predicted decadal-scale repeat rate of eruptions at the northern EPR (*10*), we initiated a 3-year OBS monitoring program in October 2003 as part of the National Science Foundation's Ridge2000 Program of coordinated research at this integrated study site (*11*). Since then, an array of up to 12 OBSs has been deployed in an ~4-by-4–km area between 9°49'N and 9°51'N, with approximately annual data recovery (Fig. 1).

The OBSs, which are deployed from a ship, each contain a seismometer that records the velocity of ground motion, a data-recording package, and an acoustic transponder that allows basic communication with the surface, including instrument release. The release system, when triggered by a coded acoustic pulse, separates the instrument from its anchor, allowing it to rise to the surface for recovery.

In the fast-spreading ridge environment, upper-crust microseismicity is dominated by small cracking events. This activity is driven largely by hydrothermal cooling (*12*) as well as stress concentrations associated with the shallow (1430 meters below the sea floor) axial magma chamber (*13*). The upper crust is therefore sensitive to crustal inflation and/or heating, as well as to increasing extensional stresses. A clear trend of increasing seismicity (*14*) from tens to many hundreds of events per day from October 2003 to May 2005 (Fig. 2) was thus interpreted as reflecting conditions within the system that were building toward an eruption (*15*). The average daily seismicity rate in 1995 was ~2.7 events per day, detected between 9°49'N and 9°51'N with a similarly designed array of nine OBSs (*12*). This activity is about one to two orders of magnitude lower than that observed from 2003 to 2006, indicating substantial differences on multiyear-to-decadal time scales, through different phases of the volcanic/tectonic cycle.

On 25 April 2006, during an expedition of the research vessel (R/V) *Knorr* to service the array, only 4 of 12 instruments were recovered (Fig. 1). Five OBSs were silent, and three were acknowledging anchor-release commands but not leaving the sea floor. In the context of the preceding years' seismicity and a pattern of instrument loss nearest the axial summit trough (AST), an eruption was immediately suspected to have occurred since the last OBS servicing in May 2005.

Corroborating evidence for this theory came from anomalies in water-column measurements of temperature and light scattering made from R/V *Knorr*. During a subsequent R/V *New Horizon* cruise (May 2006), an along-axis conductivity-temperature-depth (CTD)–optical and sample-bottle rosette tow confirmed ex-

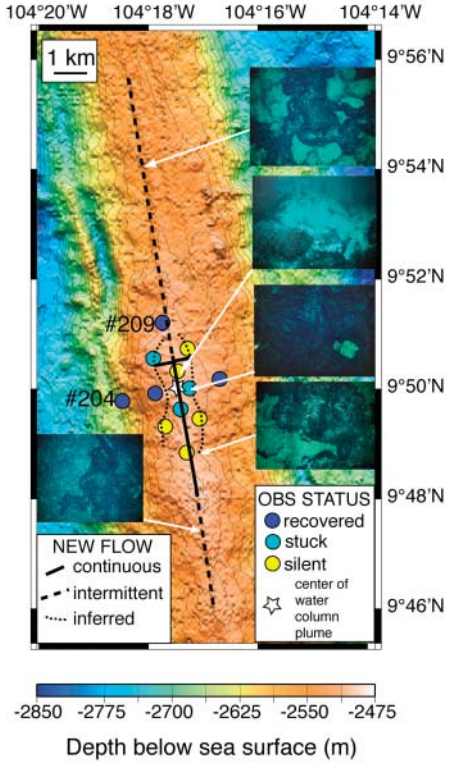


**Fig. 1.** Map of the EPR 9°50'N area (*26*) showing the OBS locations and estimated extent of the new flow. Insets are TowCam photographs showing contact relationships of the new lava flows and OBS no. 210 stuck in lava (images ~4 to 6 m across). In some locations, the on-axis new flow is continuous [e.g., 9°48′N to 9°50.5′N (solid black line)], whereas further north and south there are 50- to 200-m-long sections where it is discontinuous.

[1]Lamont-Doherty Earth Observatory (LDEO) of Columbia University, Palisades, NY 10964, USA. [2]Department of Oceanography, School of Ocean and Earth Science and Technology (SOEST), University of Hawaii at Manoa, Honolulu, HI 96822, USA. [3]Pacific Marine Environmental Laboratory (PMEL), National Oceanic and Atmospheric Administration (NOAA), WA 98115, USA. [4]Woods Hole Oceanographic Institution, Woods Hole, MA 02543, USA. [5]Department of Geology and Geophysics, University of Hawaii at Manoa, Honolulu, HI 96822, USA. [6]Department of Geological Sciences, Brown University, Providence, RI 02912, USA. [7]School of Oceanography, University of Washington, Seattle, WA 98195, USA. [8]Department of Geological Sciences, University of Florida, Gainesville, FL 32611, USA.

*To whom correspondence should be addressed. E-mail: tolstoy@ldeo.columbia.edu